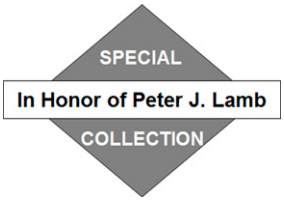

Evaluation of Snowfall Retrieval Performance of GPM Constellation Radiometers Relative to Spaceborne Radars

YALEI YOU,[a] GEORGE HUFFMAN,[b] VELJKO PETKOVIC,[a] LISA MILANI,[b,c] JOHN X. YANG,[a] ARDESHIR EBTEHAJ,[d] SAJAD VAHEDIZADE,[d] AND GUOJUN GU[a]

[a] *Department of Earth and Ocean Sciences, University of North Carolina Wilmington, Wilmington, North Carolina*
[b] *NASA Goddard Space Flight Center, Greenbelt, Maryland*
[c] *Earth System Science Interdisciplinary Center, University of Maryland, College Park, College Park, Maryland*
[d] *Department of Civil Environmental and Geo-Engineering and the Saint Anthony Falls Laboratory, University of Minnesota, Minneapolis, Minnesota*

(Manuscript received 11 April 2022, in final form 3 December 2022)

ABSTRACT: This study assesses the level-2 snowfall retrieval results from 11 passive microwave radiometers generated by the version 5 Goddard profiling algorithm (GPROF) relative to two spaceborne radars: *CloudSat* Cloud Profiling Radar (CPR) and Global Precipitation Measurement (GPM) Ku-band Precipitation Radar (KuPR). These 11 radiometers include six conical scanning radiometers [Advanced Microwave Scanning Radiometer for the Earth Observing System (AMSR-E), its successor sensor AMSR2, GPM Microwave Imager (GMI), and three Special Sensor Microwave Imager/Sounders (SSMIS)] and five cross-track scanning radiometers [Advanced Technology Microwave Sounder (ATMS) and four Microwave Humidity Sounders (MHS)]. Results show that over ocean conical scanning radiometers have better detection and intensity estimation skills than cross-track sensors, likely due to the availability and usage of the low-frequency channels (e.g., 19 and 37 GHz). Over land, AMSR-E and AMSR2 have noticeably worse performance than other sensors, primarily due to the lack of higher than 89-GHz channels (e.g., 150, 166, and 183 GHz). Over both land and ocean, all 11 sensors severely underestimate the snowfall intensity, which propagates to the widely used level 3 precipitation product [i.e., Integrated Multi-satelliteE Retrievals for GPM (IMERG)]. These conclusions hold regardless of using either KuPR or CPR as the reference, though the statistical metrics vary quantitatively. The conclusions drawn from these comparisons apply solely to the GPROF version 5 algorithm.

KEYWORDS: Algorithms; Microwave observations; Remote sensing

1. Introduction

Snowfall accounts for a significant fraction of precipitation occurrence in the middle and high latitudes (Mugnai et al. 2007; Liu 2008b; Kulie and Bennartz 2009; Behrangi et al. 2014; Skofronick-Jackson et al. 2018). Satellite remote sensing provides the only means for snowfall detection and snowfall intensity estimation on the global scale, especially over ocean where traditional gauge and ground radar observations are almost nonexistent.

Passive microwave radiometers on board multiple satellite platforms form the basis of generating the global snowfall map (Kubota et al. 2007; Huffman et al. 2015; Xie et al. 2017). Many challenging obstacles exist for snowfall detection and intensity estimation via passive microwave radiometers, including highly variable land surface emissivities, especially over the snow-covered surfaces (Mätzler 1994; Prigent et al. 2006; Noh et al. 2009; Foster et al. 2012; Takbiri et al. 2021), conflicting brightness temperature (TB) depression signature due to the ice particle scattering effect (Skofronick-Jackson and Johnson 2011; Munchak and Skofronick-Jackson 2013; You and Liu 2012; You et al. 2015) and the TB increase signature due to the supercooled liquid water emission (Kulie et al. 2010; Löhnert et al. 2011; Xie et al. 2012; Liu and Seo 2013; Wang et al. 2013; Panegrossi et al. 2017; Mroz et al. 2021), and complex radiative properties from the nonspherical ice particles and snowflakes shape (Liu 2008a; Petty and Huang 2010; Kuo et al. 2016; Eriksson et al. 2018).

Despite these challenges, radiative transfer model simulation experiments confirmed that the high-frequency channels contain snowfall detection information (Bennartz and Petty 2001; Michele and Bauer 2006; Skofronick-Jackson et al. 2004, 2013) and many previous studies demonstrated that passive microwave radiometers have the capability of detecting snowfall. For example, several snowfall detection algorithms have been developed by primarily relying on the TB depression at high-frequency channels (e.g., 183.3 GHz) for the Advanced Microwave Sounding Unit-B (AMSU-B)

Corresponding author: Yalei You, youy@uncw.edu

DOI: 10.1175/JHM-D-22-0052.1

(Staelin and Chen 2000; Chen and Staelin 2003; Kongoli et al. 2003; Noh et al. 2009; Levizzani et al. 2011). Other sensors with high-frequency channels available have also been used for snowfall detection, including Microwave Humidity Sounder (MHS) (Liu and Seo 2013; Kongoli et al. 2015; Adhikari et al. 2020), Advanced Technology Microwave Sounder (ATMS) (Kongoli et al. 2018; You et al. 2016, 2022), Special Sensor Microwave Imager/Sounder (SSMIS) (You et al. 2015), and Global Precipitation Measurement (GPM) Microwave Imager (GMI) (Kummerow et al. 2015; Rysman et al. 2018). A sensitivity study by You et al. (2017) showed that the high-frequency channels are indispensable for snowfall detection over land.

Retrieval algorithms have also been developed for snowfall intensity estimation (i.e., snowfall rate) via passive microwave observations for several sensors. Noh et al. (2006) developed a snowfall retrieval algorithm by using the airborne and ground radar snowfall rates and AMSU-B TB observations over Japan. They noticed better snowfall retrieval performance for dry and heavy snowfall events compared with wet and light snowfall events. Noh et al. (2009) applied a similar retrieval framework over the U. S. Great Lakes region. Results showed that the retrieved snowfall rate agree well with the ground radar observations when there was little snow accumulation on the ground. Snowfall retrieval algorithms have been developed for SSMIS (You et al. 2015) and ATMS (You et al. 2016) using ground radar estimates over the contiguous United States (CONUS) as the reference. It is found that the snowfall database constructed over CONUS using ground radar snowfall rates as the reference cannot be easily adapted to other regions (e.g., Tibetan Plateau and polar regions) due to the different environmental background. The Goddard profiling algorithm (GPROF) version 5 has been applied to all the passive microwave sensors in the GPM radiometer constellation (Kummerow et al. 2015). Noticeable differences were found among different sensors over the snowfall-covered land region primarily due to the availability of high-frequency channels. Meng et al. (2017) developed a 1D variational (1DVAR) snowfall retrieval algorithm over land for five passive microwave radiometers, including AMSU/MHS on board *MetOp-A*, *MetOp-B*, *NOAA-18*, and *NOAA-19* satellites and ATMS on board the *Suomi-NPP* satellite. Snowfall rates retrieved by the 1DVAR method agree well with ground radar snowfall estimates over CONUS with a correlation at ~0.5. Rysman et al. (2018, 2019) presented the snow retrieval algorithm for GMI (SLALOM) retrieval framework using coincident observations between *CloudSat* Cloud Profiling Radar (CPR) and GPM GMI. It is found that SLALOM retrieval results can capture the major snowfall bands in the Southern Ocean, and heavy snowfall events along the storm track in the Northern Hemisphere (e.g., coastal regions of North America and Greenland, Labrador Sea, western Siberia). Tang et al. (2018) concluded that the optimal snowfall retrieval performance is achieved by combining information from microwave and infrared (IR) observations and global model variables (e.g., total precipitable water).

Validation of these level-2 (i.e., swath) snowfall retrieval results is often limited to case studies (Liu and Seo 2013; Skofronick-Jackson et al. 2004; Kummerow et al. 2015; von Lerber et al. 2018; Milani et al. 2021) or over the regional scales (You et al. 2015, 2016; Meng et al. 2017; Kulie et al. 2021; Mroz et al. 2021) due to the lack of reliable ground references on the global scale. A recent study by Mroz et al. (2021) showed that the snowfall retrievals for GMI from GPROF greatly underestimate snowfall rates (by a factor of 2) compared to snowfall rates from ground radar network over CONUS. In addition, Mroz et al. (2021) also found that the probability of detection (POD) for GMI from GPROF varies from 0.1 to 0.34 over CONUS, and about 0.16 over the adjacent ocean surfaces, by using the ground radar network over CONUS. On the other hand, the POD values from SLALOM are about 0.6 over CONUS and the adjacent ocean surfaces because SLALOM used CPR snowfall estimate to build a prior database.

Similarly, snowfall validation studies for the level-3 (gridded) merged product is also limited to cases studies and over regional scales. Wen et al. (2016) noticed severe underestimation from Integrated Multi-satellitE Retrievals for GPM (IMERG) snowfall rates relative to the snowpack telemetry (SNOTEL) daily snowfall datasets over the western United States. The large underestimation from IMERG snowfall rates was also noticed over the California Sierra Nevada region by Behrangi et al. (2018) and Sadeghi et al. (2019). In contrast, Tang et al. (2020) showed that IMERG snowfall rates agree reasonably well with the ground gauge observations over mainland China, especially over the Tibetan Plateau region. Snowfall retrieval performance validation over ocean is even more limited due to the near-complete lack of reference datasets. Recently, Song et al. (2020) showed that large underestimation exists in the IMERG snowfall estimates relative to field campaign measurements over Arctic sea ice.

The objective of this study is to assess the snowfall retrieval results generated by version 5 GPROF for 11 passive microwave sensors in the GPM radiometer constellation over both land and ocean. To overcome the spatial coverage issues for validation from traditional gauge and ground radar observations, we use two spaceborne radars as the references: *CloudSat* CPR and GPM Ku-band Precipitation Radar (KuPR). CPR snowfall estimates have been widely regarded as the most reliable snowfall product available on the global scale (Kulie and Bennartz 2009; Kulie et al. 2016; Rysman et al. 2019) and are often used to construct the snowfall retrieval database for passive microwave radiometers (Liu and Seo 2013; Tang et al. 2018; Kummerow et al. 2015; You et al. 2021, 2022). The snowfall estimation performance from CPR has been validated by many previous studies. Chen et al. (2016) showed that CPR can detect about 70% of the snowfall event relative to the ground radar network over CONUS. Similarly, Mroz et al. (2021) concluded that CPR performs the best among several snowfall remote sensing instruments for snow detection with a skill score of 0.75 relative to the ground radar network over CONUS. Norin et al. (2015) showed that the detection skill score from CPR varies from 0.5 to 0.8 when comparing with ground-based weather radar network over Sweden.

Although CPR snowfall rate estimation is of high quality, CPR offer limited spatial coverage due to the nadir-view-only sampling strategy. To mitigate this challenge and further corroborate the evaluation results from CPR snowfall product, this study considers GPM KuPR snowfall rates. KuPR has

very limited capability to detect the light snowfall events (Casella et al. 2017; Panegrossi et al. 2017; You et al. 2021). Specifically, Casella et al. (2017) showed that KuPR can only detect about 7% of snowfall occurrence and about 30% of snowfall amount, relative to CPR observations. Using the ground radar network over CONUS, Mroz et al. (2021) showed that KuPR is able to detect about 31% of the snowfall events. However, KuPR has a much wider spatial coverage (~245 km from KuPR versus ~2 km from CPR) and is currently operational. Similar strategies (i.e., using spaceborne radar as the reference) have also been used to evaluation the rainfall retrieval performance for multiple sensors (Lin and Hou 2008; You et al. 2020).

Although we take CPR and KuPR as the references to assess the snowfall retrieval performance of these passive microwave radiometers, neither of the spaceborne radars is perfect for snowfall measurement. For example, spaceborne radars provide the snowfall estimates near the surface, which is defined as the surface closest to the ground without ground clutter. Specifically, *CloudSat* defines the near-surface bin height as the sixth (fifth) range gate above land (ocean) surfaces or about 1.44 (1.2) km above ground (sea) level. On the other hand, KuPR is a scanning radar with the near-surface bin ranging from ~1 km (nadir and near-nadir scans) to ~2.5 km (furthest off-nadir scans) above ground/sea level. Therefore, both spaceborne radars may miss the shallow snowfall systems below the near surface height.

2. Data

a. CPR and KuPR snowfall rate products

This study uses snowfall rates estimated from *CloudSat* CPR and GPM KuPR as the references. CPR is a 94-GHz nadir-looking radar with a footprint size of 1.4 km × 1.8 km (Stephens and Kummerow 2007). We obtain the surface snowfall rate from the V05 (latest version) 2C-SNOW-PROFILE product. KuPR is a cross-track scanning radar on board the GPM *Core Observatory* with a nadir resolution of about 5.2 km and swath width of ~245 km. We obtain the variable "precipRateNearSurface" from the V06 (latest version at the time of writing this manuscript) 2A-DPR product for KuPR.

Precipitation phase parameter (i.e., rainfall, snowfall, and mixed) in the KuPR product is determined at the near-surface bin height (~1.5 km above the surface), which is the height closest to the ground without the ground clutter. Previous studies showed that snowfall occurrence is greatly overestimated by using the phase determination directly from KuPR (Skofronick-Jackson et al. 2019; You et al. 2021) because precipitation phase may change from solid to liquid when falling from the near-surface height (~1.5 km) to the ground. For this reason, we use the precipitation phase determination method from Sims and Liu (2015). Several separation schemes were developed by Sims and Liu (2015) requiring different input variables (e.g., 2-m air temperature, 2-m wet bulb temperature, pressure, etc.) This study uses the 2-m wet-bulb temperature from Modern-Era Retrospective Analysis for Research and Applications, version 2 (MERRA-2; Gelaro et al. 2017) as the input variable over both land and ocean. To largely exclude the possible mixed phase precipitation, we only select the KuPR pixels with the snowfall probability greater than 90%. To be consistent with KuPR phase determination, we also apply the same threshold value (i.e., snowfall probability greater than 90%) for the CPR snowfall product.

b. GPROF snowfall estimates from 11 radiometers

This study uses the precipitation estimates from 11 passive microwave sensors, including AMSR-E on board the *Aqua* satellite; AMSR2 on board the *GCOM-W1* satellite; GMI on board the GPM *Core Observatory* satellite; SSMIS on board *F16*, *F17*, and *F18* satellites; ATMS on board the *Suomi-NPP* satellite; MHS on board *MetOp-A*, *MetOp-B*, *NOAA-18*, and *NOAA-19* satellites. For simplicity and convenience, these sensors are referred to as AMSR-E, AMSR2, GMI, SSMIS-*F16*, SSMIS-*F17*, SSMIS-*F18*, ATMS, MHS-*MA*, MHS-*MB*, MHS-*N18*, and MHS-*N19*. From now on, we use these abbreviations to represent either the sensors themselves or the GPROF retrieved precipitation rates from these sensors, depending on the context of discussion. In the precipitation community, these 11 sensors are commonly grouped into two categories: conical scanning and cross-track scanning sensors. Cross-track scanning radiometer is the sensor with varying footprint size across the scan line, including ATMS and MHS. In contrast, the footprint size remains unchanged across the scan line for the conical scanning radiometer, including AMSR-E, AMSR2, GMI, and SSMIS. Some of the diurnal cycle differences among these sensors may be difficult to capture through the direct comparison approach presented in this study.

Precipitation rates for all 11 sensors are generated by version 5 GPROF (Kummerow et al. 2015). GPROF uses the Bayesian framework to estimate the precipitation rate based on the observed microwave brightness temperatures from the passive sensors. Specifically, GPROF builds the retrieval database primarily using GMI brightness temperatures and KuPR rain rates (filling in with ground radar precipitation estimates over snow-covered surfaces) to constrain the precipitation vertical profile. To further constrain the solution, GPROF stores the a priori information into so-called databases, subsetted by surface type and environmental conditions (e.g., total precipitable water and 2-m temperature). For each satellite pixel, GPROF provides both the precipitation rate and an estimate of the frozen precipitation rate as a linear product of the precipitation rate and an estimated snowfall probability (Sims and Liu 2015). This study chooses to use the precipitation rate as the "snowfall rate" whenever the snowfall probability is greater than 0.90, effectively limiting the evaluation analyses to snowfall cases.

GPROF retrieves precipitation over 14 surface types, including ocean, sea ice, five vegetation types, four snow-covered types, standing water, water–land boundary (coast), and water–sea ice boundary. This study combines vegetation and snow-covered surface types into the single "land" type. We only assess GPROF snowfall retrieval performance over ocean and land surface types since there are limited snowfall samples over other surface types (except over sea ice). Over sea ice, we examined the GPROF snowfall retrieval results but do not show them in the current study primarily due to the relatively poor retrieval

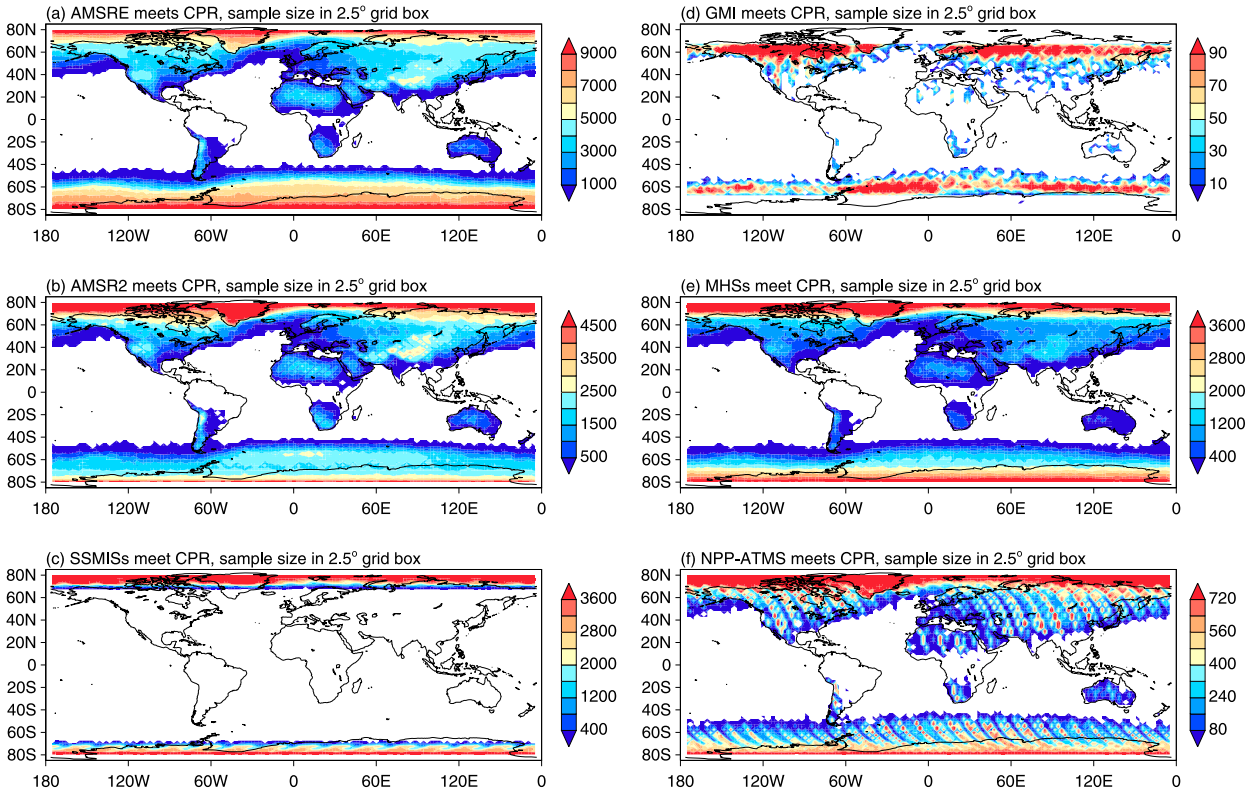

FIG. 1. Coincident observation count between *CloudSat* CPR and each passive microwave sensor, including (a) AMSR-E; (b) AMSR2; (c) three SSMISs on board *F16*, *F17*, and *F18* satellites; (d) GMI; (e) four MHSs on board *MetOp-A*, *MetOp-B*, *NOAA-18*, and *NOAA-19*; and (f) ATMS in 2.5° grid boxes. CPR data are from June 2006 to July 2019 and the coincident matchups are obtained when passive microwave data are available in the same period. Only the matchups associated with possible snowfall [i.e., snowfall probability greater than 90% based on Sims and Liu (2015)] are shown.

performance of the current GPROF version (version 5). In addition, there are limited sea ice samples over the region covered by GMI in the Northern Hemisphere.

For different sensors, GPROF uses different channel sets for snowfall retrieval. The channel set used over land and ocean also differs. Specifically, for conical scanning sensors, all available channels from 10 to 183 GHz are utilized over land, while only channels from 10 to 89 GHz when available are used over ocean. For cross-track radiometers, only the high-frequency channels (from 89 to 183 GHz) from ATMS and MHS are used, with 89 GHz being considered the most important channel in the snowfall rate estimation process. As shown later, these channel selection schemes have important implications for the retrieval performance. The channel sets used for precipitation retrieval from each sensor can be found in Table 1 of You et al. (2020).

c. *Temporal and spatial coverage*

We use the full CPR snowfall product record from June 2006 to July 2019 over the *CloudSat* covered region of ~82°S–82°N. It is noted that *CloudSat* satellite is in day-only operation mode since November 2011, which has little influence on the evaluation results in this study (Milani and Wood 2021). We obtain the coincident observations between CPR and all passive microwave sensors when a pair pixel from CPR and each sensor is no more than 10 km apart and no more than 10 min away from each other. To increase the sample size between CPR and SSMIS, coincident observations between SSMIS on board three satellites (i.e., *F16*, *F17*, and *F18*) and CPR are combined (discussed in section 4). Similarly, coincident observations from four MHSs (i.e., *MetOp-A*, *MetOp-B*, *NOAA-18*, and *NOAA-19*) and CPR are combined. For either AMSR2 or AMSR-E, there are enough coincident samples with CPR because of the close orbit formation between *CloudSat* and *GCOM-W1*, and between *CloudSat* and *Aqua*. Therefore, the coincident observations for AMSR-E and AMSR2 are not combined.

We use the GPM KuPR snowfall product from March 2014 to December 2020 over the latitude band observed by GPM (~65°S–65°N) to obtain the coincident observations between KuPR and all passive microwave sensors except for AMSR-E, which stopped functioning in October 2011 and therefore has no overlap observation period with KuPR. The threshold values for the coincident observations between KuPR and each sensor are set at 5 km apart and 5 min away from each other. These threshold values for CPR and KuPR are chosen by considering the trade-off between the sample size and the robustness of the evaluation results.

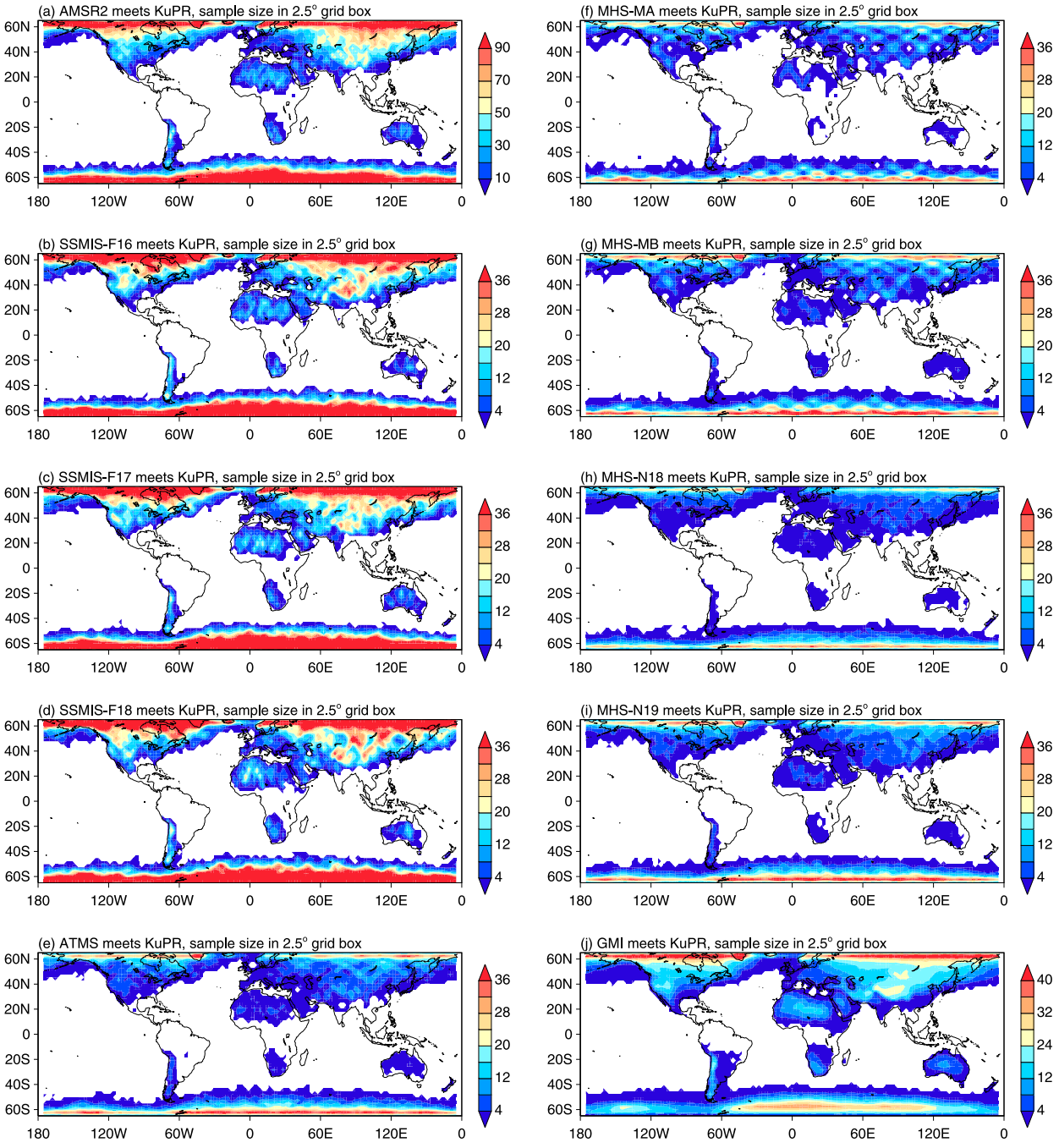

FIG. 2. Coincident observation count between GPM KuPR and each passive microwave sensor, including (a) AMSR2, (b) SSMIS-*F16*, (c) SSMIS-*F17*, (d) SSMIS-*F18*, (e) ATMS, (f) MHS-*MA*, (g) MHS-*MB*, (h) MHS-*N18*, (i) MHS-*N19*, and (j) GMI in 2.5° grid boxes. The number is scaled by 100 in each plot except for in (j) where the number is scaled by 10 000 (note that GMI and KuPR are on the same satellite platform, i.e., GPM *Core Observatory*). The data are from March 2014 (just after the launch of the GPM satellite) to December 2020 except for MHS-*N18*, which ends in October 2018 when *NOAA-18* stopped functioning. Only the matchups associated with possible snowfall [i.e., snowfall probability greater than 90% based on Sims and Liu (2015)] are shown.

3. Methodology

a. Collocation scheme

GPROF retrieved snowfall rates for AMSR-E/AMSR2, SSMIS and GMI are provided at their ~19-GHz channel resolutions, which are approximately 21, 59, and 15 km, respectively. For MHS and ATMS, the nominal resolution for the retrieved surface precipitation rate is ~16 km at nadir. GPROF does not produce retrieval results for several pixels near the edges of each scan line for ATMS and MHS, which

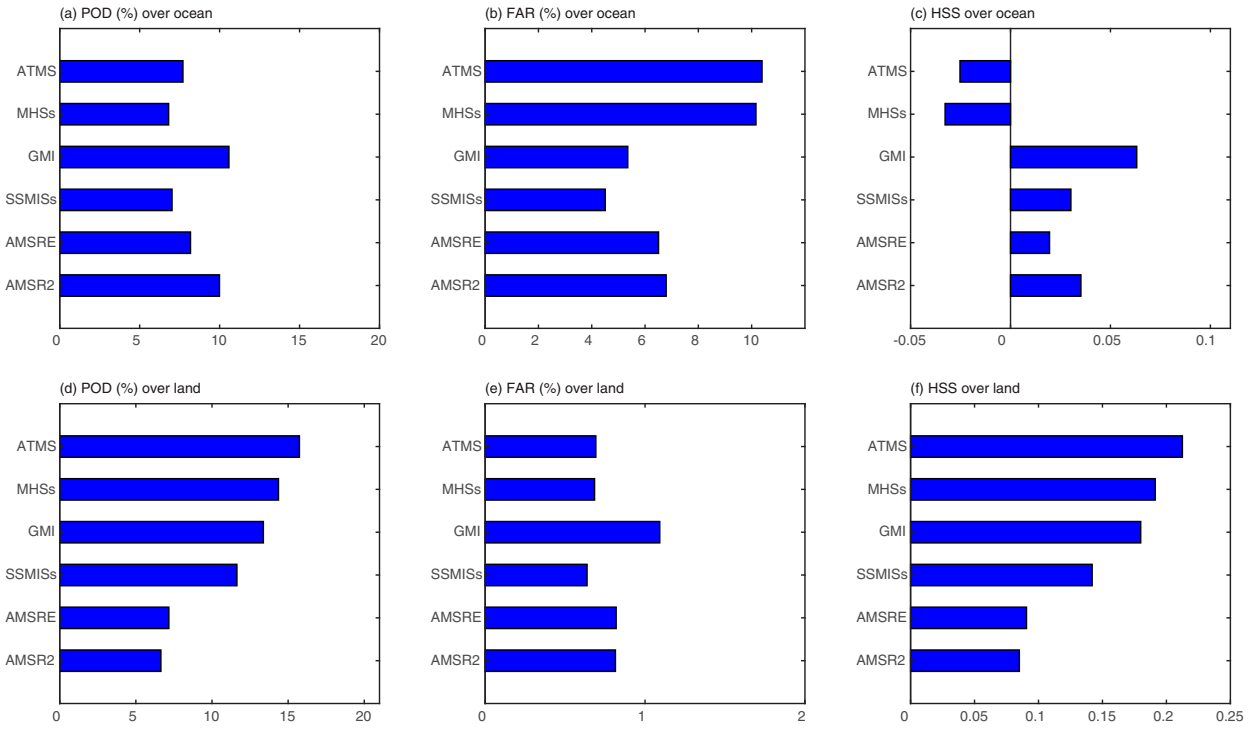

FIG. 3. (a) Probability of detection (POD), (b) false alarm rate (FAR), and (c) Heidke skill score (HSS) over ocean for AMSR2; AMSR-E; three SSMISs on board *F16*, *F17*, and *F18* satellites; GMI; four MHSs on board *MetOp-A*, *MetOp-B*, *NOAA-18*, and *NOAA-19*; and ATMS over ocean based on CPR from June 2006 to July 2019. (d)–(f) As in (a)–(c), but over land. Note that the FAR [in (b) and (e)] and HSS [in (c) and (f)] values over land and ocean have different *x*-axis scales.

mitigates the negative impact of the large footprint size at the edge of the scan line.

For retrieval results from the radiometers, we use their native retrieval resolutions. As mentioned previously, the retrieval resolutions from all sensors are close to 15-km nominal resolution, except that from SSMIS (59 km). This study takes 15 km as the nominal resolution. To match KuPR and CPR spatial resolution to that of SSMIS, full-resolution KuPR and CPR must be averaged over several pixels. The snowfall rate from KuPR has a spatial resolution of ~5 km. We simply average 3 × 3 KuPR pixels to achieve 15 km × 15 km resolution. Specifically, we take the arithmetic mean of the precipitation rates from KuPR every three pixels in both the cross and along scan line directions. Since CPR provides the nadir only observation with a spatial resolution of ~1.7 km, we simply average 9 (15/1.7 = 9) pixels along the scan line to mitigate the clear resolution discrepancy between CPR and GPROF retrieval results' spatial resolution. Our previous studies showed that the statistical values (e.g., correlation) will change when different nominal resolution is used, however, the retrieval performance's relative ranking from passive microwave radiometers remains (You et al. 2020).

b. *Snowfall detection evaluation metrics*

To assess the snowfall detection performance, we compute four numbers in a 2 × 2 contingency table (hit, miss, false alarm, and correct negative; Wilks 2011). These four numbers are referred to, in order, *a*, *b*, *c*, and *d*. In the following definitions regarding the detection evaluation metrics, we take the coincident observations from CPR and AMSR-E as an example. This definition is equally applicable to the other sensors and when KuPR is taken as the reference.

A hit is defined as both the reference (CPR) and the AMSR-E retrieval detecting snowfall. A false alarm is when the AMSR-E detects snowfall while CPR does not, while a miss is when CPR detects snowfall but AMSR-E does not. A correct negative is when both CPR and AMSR-E detect no snowfall.

This study uses 0.2 mm h^{-1} as the snow/nonsnow threshold value because 1) previous study showed that passive microwave radiometers' detection limitation is around 0.2 mm h^{-1} (Munchak and Skofronick-Jackson 2013) and 2) GPROF retrieval results below 0.2 mm h^{-1} are poor. In fact, it is noticed that GPROF retrieval algorithm generates many light snowfall rate values around 0.1 mm h^{-1} corresponding to CPR snowfall rates from 0.05 to 1 mm h^{-1}. This feature may indicate that snowfall rate lighter than 0.2 mm h^{-1} is beyond the passive microwave radiometers' detection limitation in the GPROF retrieval framework. We also calculate the detection statistics using other threshold values (e.g., 0.1 mm h^{-1}), but the rank of these passive microwave radiometers does not change with different threshold values (not shown).

This study computes the detection accuracy metrics derived from the aforementioned four numbers, including probability of detection (POD), false alarm rate (FAR), and Heidke skill score (HSS). These metrics are calculated as follows:

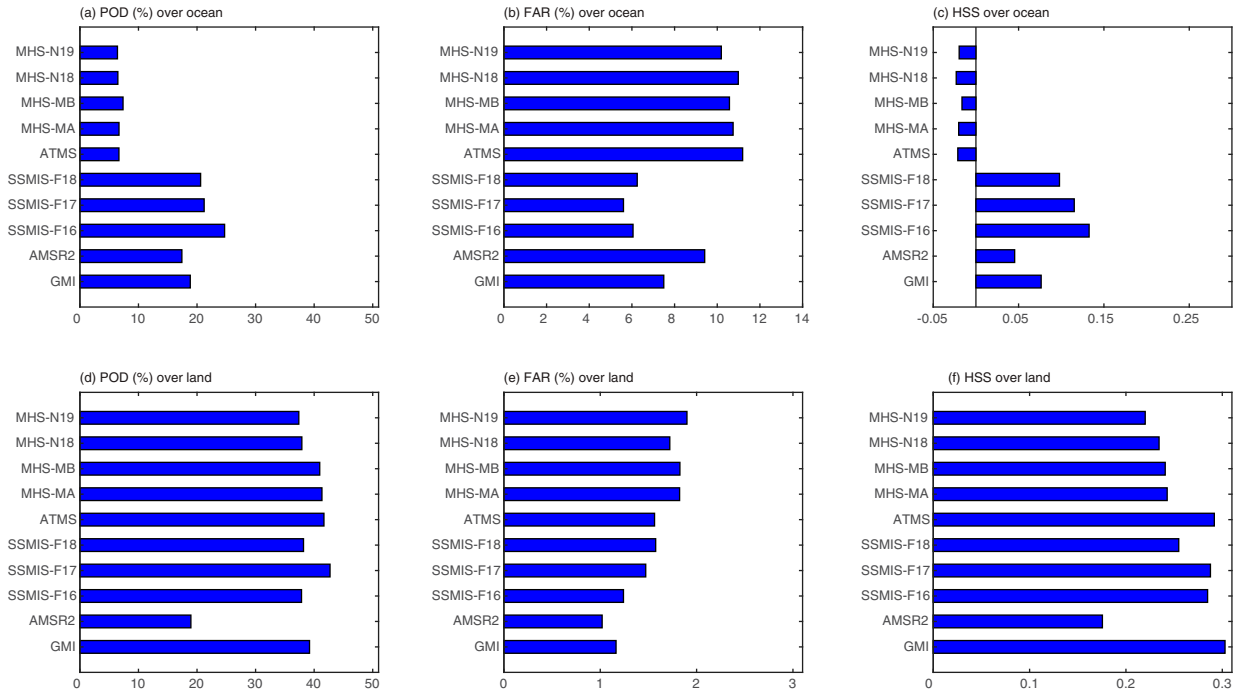

FIG. 4. (a) POD, (b) FAR, and (c) HSS over ocean for GMI, AMSR2, SSMIS-*F16*, SSMIS-*F17*, SSMIS-*F18*, ATMS, MHS-*MA*, MHS-*MB*, MHS-*N18*, and MHS-*N19* based on GPM KuPR from March 2014 to December 2020, except MHS-*N18* ends in October 2018. (d)–(f) As in (a)–(c), but over land. Note that the FAR [in (b) and (e)] and HSS [in (c) and (f)] values over land and ocean have different *x*-axis scales.

$$\mathrm{POD} = \frac{a}{a + c},$$

$$\mathrm{FAR} = \frac{b}{b + d},$$

$$\mathrm{HSS} = \frac{2(ad - bc)}{(a + c)(c + d) + (a + b)(b + d)}. \quad (1)$$

A large POD value is often associated with a large FAR value, which makes it difficult to assess detection performance using POD or FAR alone. This study uses the HSS (varying from −1 to +1) value to judge the overall detection performance. HSS is a generalized skill score that quantifies how well AMSR-E detects precipitation compared to random chance. An HSS value greater than zero indicates a performance better than random chance.

c. *Snowfall intensity evaluation metrics*

Similar to the detection evaluation metrics definition, we take the coincident observations from CPR and AMSR-E as an example, and the definition is equally applicable to the other sensors and when KuPR is taken as the reference. When both CPR and AMSR-E detect snowfall, we also compute the correlation coefficient between CPR and AMSR-E.

To further evaluate the snowfall intensity, we compute the normalized bias (nBIAS) and normalized root-mean-square-error (nRMSE) in different CPR snowfall intensity bins (Lin and Hou 2008; Tang et al. 2014; You et al. 2020). Without binning the snowfall intensity, these two metrics are weighed toward the most frequently light-snowfall pixels when computing these statistical measures (Conner and Petty 1998; Lin and Hou 2008). In each intensity bin (e.g., 0.2–0.5 mm h^{-1}), these two metrics are computed:

$$\mathrm{nBIAS} = \frac{\frac{1}{n}\sum_{i=1}^{n}(y_i - x_i)}{\overline{x}},$$

$$\mathrm{nRMSE} = \frac{\sqrt{\frac{1}{n}\sum_{i=1}^{n}(y_i - x_i)^2}}{\overline{x}}, \quad (2)$$

where x_i and y_i are the CPR snowfall rate and AMSR-E snowfall rate, respectively. The $\overline{x}$ and n represents the mean CPR snowfall rate and sample size in that particular bin. Both the zero and nonzero snowfall rates from the coincident AMSR-E precipitation rates are included.

4. Results

a. *Geospatial distribution of the coincident observations*

The geospatial distribution of the coincident observations between passive microwave sensors and CPR varies greatly due to the different orbit formations (Yang et al. 2016). Because *CloudSat* satellite with CPR on board and *Aqua* satellite with AMSR-E on board are both in the A-Train constellation and only several minutes (mainly about 1 min) apart from each other, there are many more coincident matchups between CPR and AMSR-E (cf. Fig. 1a and other subplots in Fig. 1). Due to the close orbit formation of *CloudSat* with

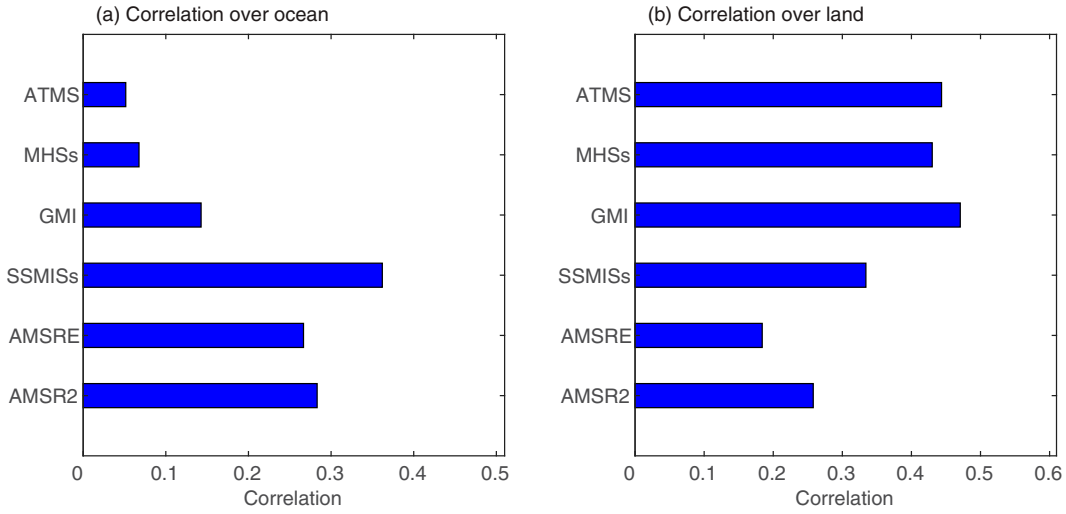

FIG. 5. (a) Correlation between coincident snowfall rate observations from CPR and from each sensor over ocean from March 2014 to July 2019. (b) As in (a), but over land.

GCOM-W1, *NOAA-18*, and *NOAA-19*, the geospatial distribution of the coincident observations between CPR and AMSR2, and between CPR and MHSs are similar to that from AMSR-E, although the sample sizes are smaller (cf. Figs. 1a,b, cf. Figs. 1a,e). In contrast, the coincident observations from other three sensors are restricted to smaller geospatial region and with noticeably less samples. Especially, the coincident matchup from SSMISs and CPR are mostly located poleward of 70°S/N. The different geospatial coverage from these coincident observations can affect the comparison results (more discussion later).

Different from the geospatial distribution from CPR (Fig. 1), the geospatial coverage of coincident observations from KuPR and each passive microwave sensor is similar among these matchups (Fig. 2), although the sample size differs greatly. Analysis in section 4 shows that the sample size variation among these sensors does not change the sensor performance rank. In addition, the similar geospatial coverage of the matchups of different sensors with KuPR produces a more stable comparison than the matchups with CPR.

b. *Snowfall detection performance*

Snowfall detection performance assessed against CPR reveals that the overall detection skills over ocean are weak for all the passive microwave sensors. Figure 3a shows that POD values from all the sensors are lower than 12%, and the FAR values are similar (cf. Figs. 3a,b). That is, over ocean the correctly detected snowfall pixel numbers (i.e., snowfall indeed occurs according to the reference) and the falsely detected snowfall pixel numbers (i.e., no snowfall occurs according to the reference) are similar. Therefore, the overall HSS skill scores are very low for all sensors. More specifically, the HSS values for cross-track scanning radiometers (MHSs and ATMS) are slightly negative (overall detection skills are less than the random chance) and slightly positive for conical scanning radiometers (better than random chance skill). The slightly higher HSS value from GMI than those from other conical scanning sensors (AMSR-E, AMSR2, and SSMISs) arises because matchups from GMI and CPR are only available in the latitude band 65°S/N. When AMSR2 and AMSR-E matchups are restricted to this smaller zone (i.e., the GPM covered region), the HSS values from AMSR2/AMSR-E are very close to the GMI HSS.

As mentioned previously, only high-frequency channels (89–183 GHz) from MHSs are available for snowfall detection over ocean. To be consistent, only the high-frequency channels from ATMS are used, even though the low-frequency channels (e.g., 23–31 GHz) are available from ATMS. For conical scanning radiometers (GMI, AMSR-E, AMSR2, and SSMISs), channels from 10 (when available) to 89 GHz are used. Comparing the detection performance from conical scanning radiometers and cross-track scanning radiometers (e.g., AMSR2 versus ATMS), it is concluded that the low-frequency channels contain additional information for snowfall detection. Therefore, it is suggested that the low-frequency channels from ATMS should be used. Also, the same satellite platforms that carry MHS sensors also carry AMSU-A, with low-frequency channels. It is suggested that the low-frequency channels from AMSU-A should be paired with MHS to enhance the snowfall detection performance. In addition, we also analyzed the snowfall detection performance by using the pixels near the nadir scans from ATMS and MHS, which have comparable resolution with SSMIS, and more importantly, whose corresponding atmospheric columns coincide with that of the reference radar. The HSS values remain smaller than those from conical scanning radiometers, indicating that the varying footprint size from cross-track scanning radiometers is not the primary reason why cross-track scanning radiometers have a worse performance than conical scanning radiometers.

Over land, sensors with higher-frequency channels (e.g., 150, 166, and 183 GHz) including GMI, SSMISs, MHSs, and

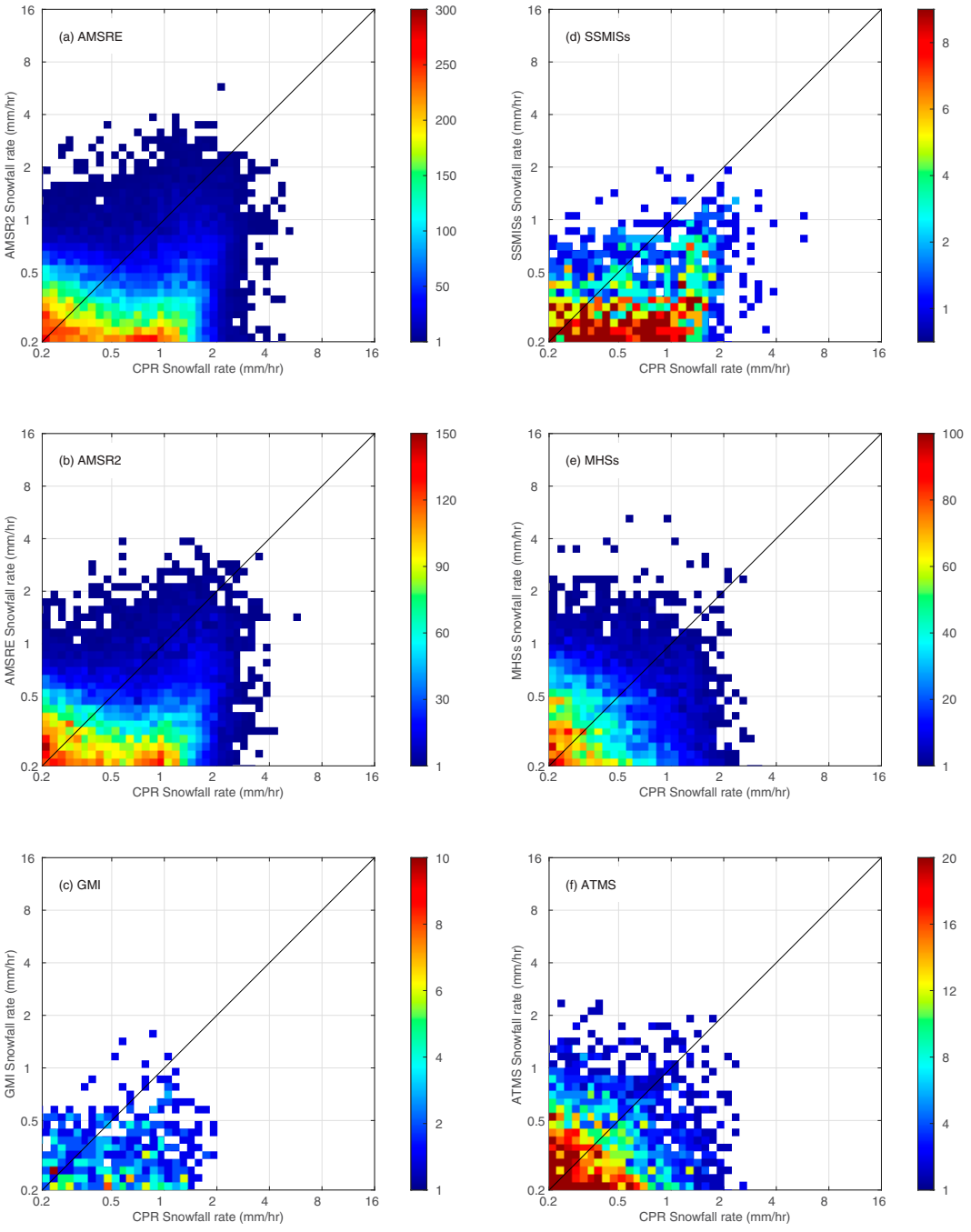

FIG. 6. Scatterplots between coincident CPR snowfall rates and snowfall rates from passive microwave sensors over ocean for March 2014–July 2019: (a) AMSR-E; (b) AMSR2; (c) GMI; (d) three SSMISs on board DMSP *F16*, *F17*, and *F18*; (e) GMI; (f) four MHSs on board *MetOp-A*, *MetOp-B*, *NOAA-18*, and *NOAA-19*; and (g) ATMS.

ATMS have POD values at about 14% (Fig. 3d), while POD values from AMSR-E and AMSR2 with highest frequency up to 89 GHz are only about 7% (Fig. 3d). At the same time, all sensors have a FAR value at about 1% (Fig. 3e), giving the overall detection skills from SSMISs, GMI, MHSs, and ATMS that are higher than those from AMSR2 and AMSR-E (Fig. 3f). Also, Fig. 3f shows that the HSS value from SSMISs is noticeably smaller than those from GMI, MHSs, and ATMS, which arises because the coincident observations from SSMISs and CPR are located at 70°S/N poleward. When the matchups from ATMS and MHSs are restricted to poleward of 70°S/N, the HSS values are almost identical to that from SSMISs, indicating the importance of geospatial distribution.

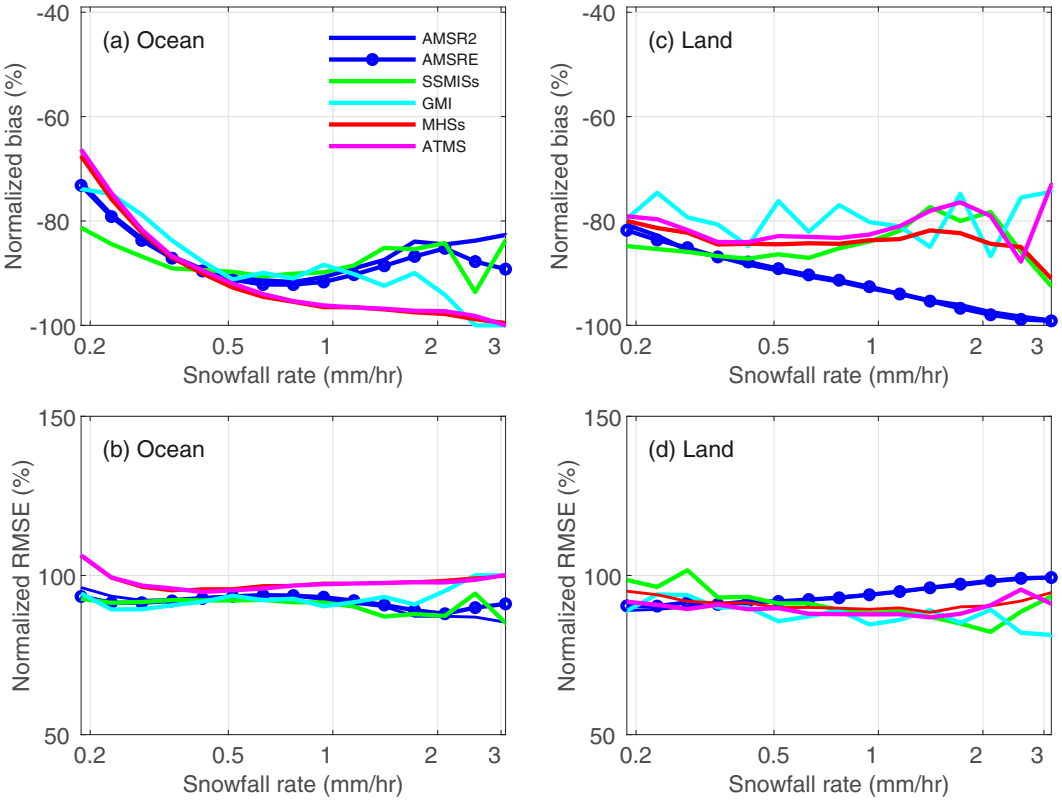

FIG. 7. (a) Normalized biases as a function of the CPR snowfall intensity over ocean for the period March 2014–July 2019. (b) As in (a), but for normalized RMSE. (c) As in (a), but over land. (d) As in (b), but over land. The legend for all panels is shown in (a).

The conclusions using GPM KuPR for the snowfall detection evaluation are highly consistent with those from CPR over both land and ocean. That is, over ocean HSS values for all cross-track scanning radiometers (ATMS and four MHSs) are slightly negative while conical scanning radiometers (GMI, SSMISs, and AMSR2) have small positive HSS values (Fig. 4c). Notice that the HSS values from AMSR2 and GMI are smaller than those from SSMISs over ocean. The most likely reason may be the finer footprint size of AMSR2 and GMI, making them prone to false detection of more snowfall events (i.e., larger FAR, Fig. 4b). Over land, AMSR2 has noticeably smaller POD (Fig. 4d) and HSS (Fig. 4f) values because higher-frequency channels (e.g., 150 and 183 GHz) are not available from AMSR2.

c. *Snowfall intensity performance*

The snowfall intensity analysis (which only considers matchups with snowfall rate ≥ 0.2 mm h^{-1}) relative to CPR shows that conical scanning radiometers have greater correlation with CPR snowfall rates than cross-track scanning radiometers over ocean (Fig. 5a). GPROF uses all channels from 89 to 183 GHz from MHS and ATMS snowfall intensity estimation, although the weight in the Bayesian retrieval framework for 89 GHz is much larger than those for other channels, meaning that the retrieval heavily relies on information from the 89-GHz channel. In contrast, all channels from ~10 GHz (when available) to 89 GHz are used in the snowfall intensity estimation process for conical scanning radiometers, with more weights being assigned to low-frequency channels (10, 19, and 37 GHz). The usage of the low-frequency channels is responsible for the better correlation from conical scanning radiometers. Additionally, GMI has a smaller correlation compared to SSMISs, AMSR-E, and AMSR2. This is caused by the geospatial distribution of the coincident observations between GMI and CPR, which are mostly from the Southern Ocean (Fig. 1d). Therefore, these matchups miss heavy snowfall events over the storm tracks in the Northern Hemisphere (e.g., coastal regions of North America and Greenland, and the Labrador Sea).

The scatter density plot corroborates the better performance from conical scanning radiometers (Fig. 6). For example, cross-track scanning radiometers underestimate the snowfall rates to a larger degree when CPR snowfall rates are greater than 1 mm h^{-1} (cf. Fig. 6b for AMSR2 and Fig. 6e for MHSs). The larger underestimates from cross-track scanning radiometer are more evident in Fig. 7a for snowfall rate greater than 1 mm h^{-1} (red and purple curves). Clearly, the sample size for GMI matchups with CPR is limited, shown in Fig. 6c. In fact, only several GMI snowfall rates are greater than 1 mm h^{-1} in the matchup dataset, which greatly reduces

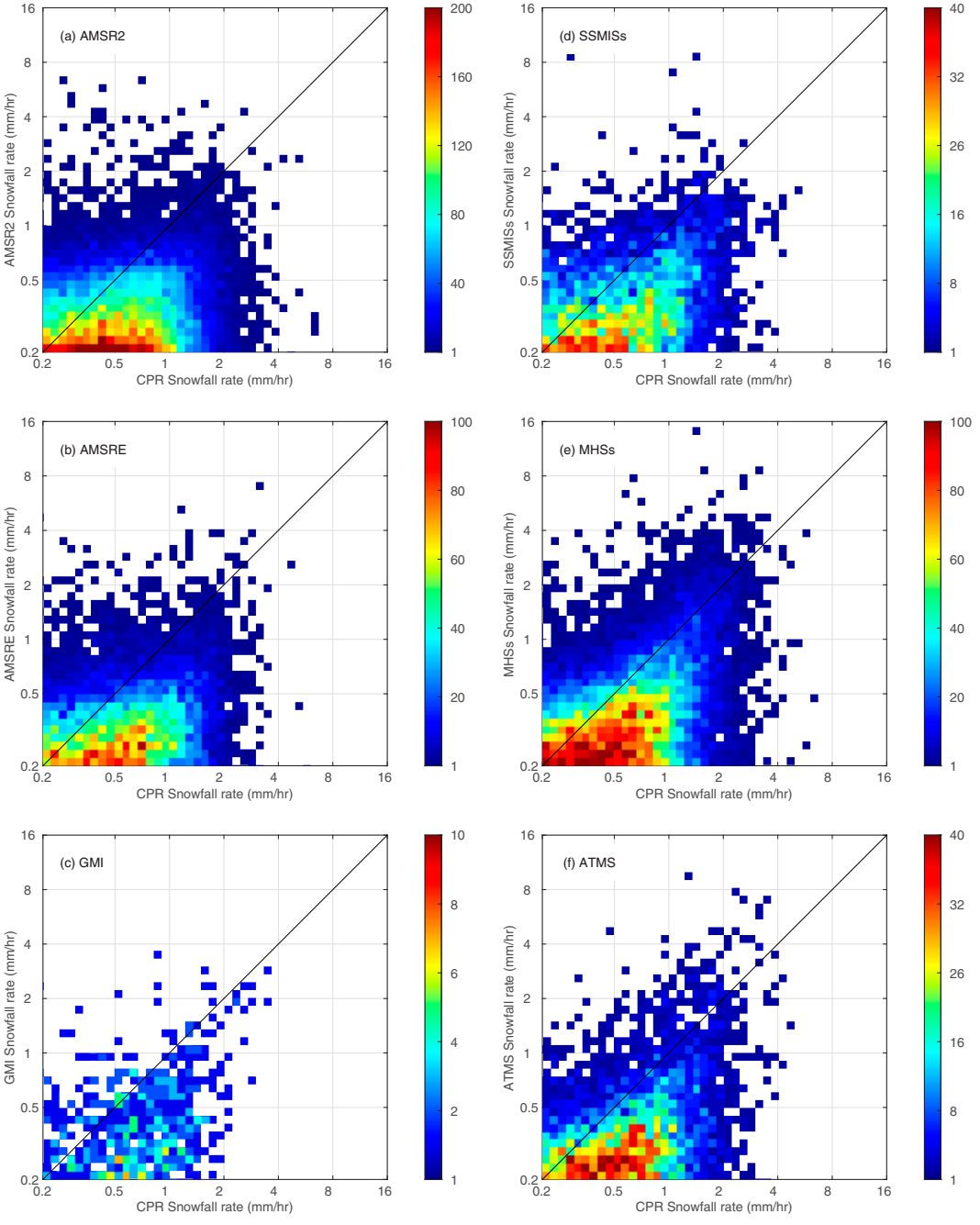

FIG. 8. As in Fig. 6, but for land.

the correlation between CPR and GMI. This is the reason why GMI has smaller correlation compared with SSMISs, AMSR-E, and AMSR2 (Fig. 5a). The RMSE from each senor is similar over ocean, shown in Fig. 7b.

Over land, AMSR-E and AMSR2 have smaller correlation with CPR than the sensors with higher-frequency channels available (e.g., 150, 166, and 183 GHz), including GMI, MHSs, SSMISs, and ATMS (Fig. 5b). This result is not surprising since these higher-frequency channels are essential for snowfall retrieval over land, which are more sensitive to ice particle scattering than other channels (e.g., 19, 37, and 89 GHz) and less affected by the underlying surface properties (Grody 1991; Skofronick-Jackson and Johnson 2011; Kummerow et al. 2015; You et al. 2015). The better correlation performance is also evident from the scatterplot (Fig. 8). The slightly smaller correlation from SSMISs than GMI, MHSs, and ATMS is due to matchups being limited to poleward of 70°S/N. When MHSs and ATMS are restricted to the

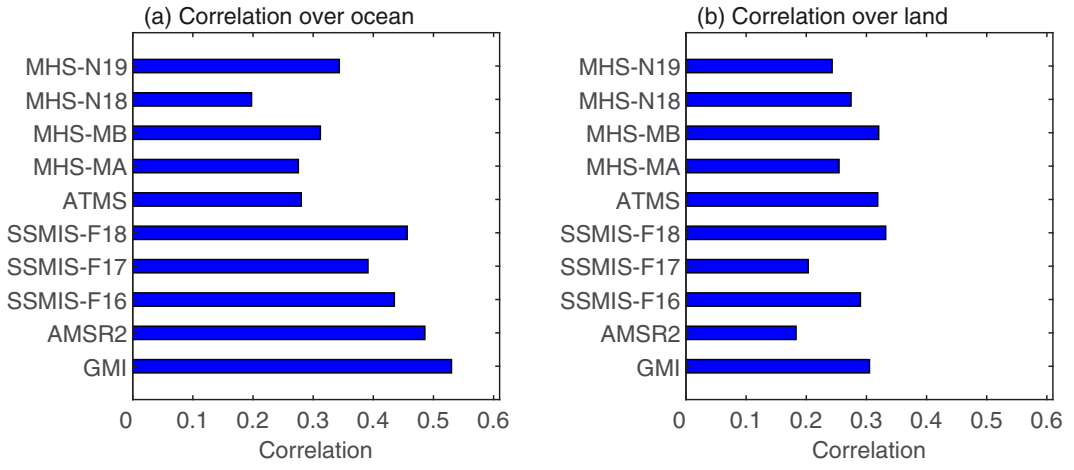

FIG. 9. (a) Correlation between coincident snowfall rate observations from KuPR and from each sensor over ocean for March 2014–December 2020, except MHS-*N18* ends October 2018. (b) As in (a), but over land.

same regions, the correlations from these three types of sensors (i.e., SSMIS, MHS, and ATMS) are almost identical. The larger underestimation from AMSR-E and AMSR2 is obvious from the bias plot in Fig. 7c. It is also worth mentioning that all sensors greatly underestimate the snowfall intensities (Fig. 7c). This large underestimation feature clearly propagates into the level 3 merged precipitation product, as noticed by previous studies (Wen et al. 2016; Behrangi et al. 2018; Sadeghi et al. 2019). Similar to RMSE over ocean, no clear difference is noticed for RMSE among these sensors over land (Fig. 7d).

Intensity analyses based on KuPR generates results that are very consistent with those based on CPR. Figure 9a shows the correlation between KuPR and each sensor over ocean. It is immediately clear that conical scanning radiometers have higher correlation than cross-track scanning radiometers. In this case, GMI actually has the largest correlation among the conical scanning radiometers, which is further evidence that the smaller correlation from GMI (Fig. 5a) with CPR is due to the geospatial distribution of the matchup dataset. The better performance from conical scanning radiometers is also evident from the scatterplots (Fig. 10) and bias analysis. Especially, Fig. 11a shows that all conical scanning radiometers have relatively smaller negative bias than those from cross-track scanning radiometers. As explained earlier in the CPR

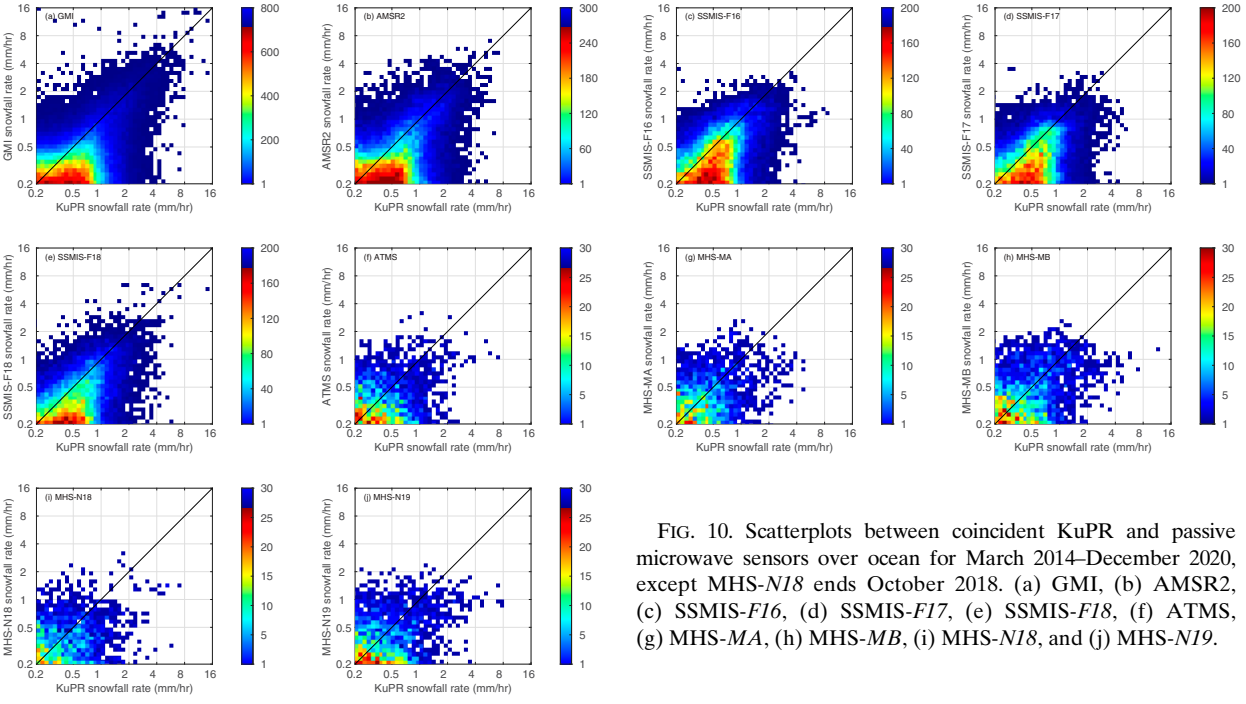

FIG. 10. Scatterplots between coincident KuPR and passive microwave sensors over ocean for March 2014–December 2020, except MHS-*N18* ends October 2018. (a) GMI, (b) AMSR2, (c) SSMIS-*F16*, (d) SSMIS-*F17*, (e) SSMIS-*F18*, (f) ATMS, (g) MHS-*MA*, (h) MHS-*MB*, (i) MHS-*N18*, and (j) MHS-*N19*.

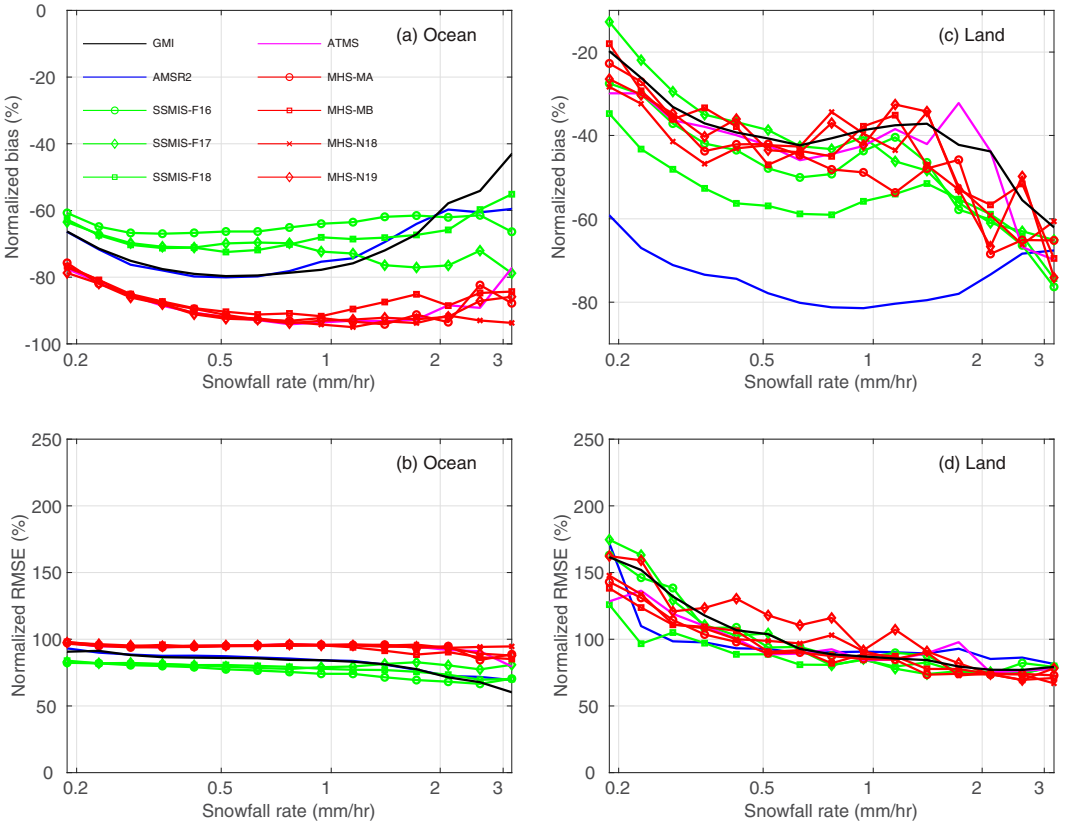

FIG. 11. (a) Normalized biases as a function of the KuPR snowfall intensity over ocean. (b) As in (a), but for normalized RMSE. (c) As in (a), but over land. (d) As in (b), but over land. The legend for all panels is shown in (a).

analysis, the better performance from conical scanning radiometers arises because of the usage of the low-frequency channels.

The analyses against KuPR over land are also very consistent with the CPR results. Notice that AMSR2 has lower performance than other sensors. For example, there are more snowfall rates with intensities greater than 0.5 mm h^{-1} from SSMIS-*F16* (Fig. 12c) than that from AMSR2 (Fig. 12b). Also, a much larger underestimation is evident from AMSR2 in Fig. 11c. Similar to analysis based on CPR, the RMSE over both land and ocean remains comparable among all sensors (Figs. 11b,d).

5. Conclusions and discussions

This study assesses the snowfall retrieval results from 11 sensors in the GPM radiometer constellation, by using *CloudSat* CPR and GPM KuPR as references. These 11 radiometers include six conical scanning radiometers and five cross-track scanning radiometers. Although the statistical values for both detection and intensity estimation vary when using CPR and KuPR as references, major conclusions are highly consistent over both land and ocean, regardless of the reference. These major conclusions are as follows:

1) Over ocean, conical scanning radiometers have greater detection skills and better correlate with the snowfall rates from references (both KuPR and CPR). The primary reason why conical scanning sensors perform better is because they use the low-frequency channels.
2) Over land, sensors with higher-frequency channels (150, 166, and 183 GHz), including GMI, SSMISs, MHSs, and ATMS, perform noticeably better than AMSR-E and AMSR2 (whose highest available frequency is ~89 GHz) in terms of both snowfall detection and snowfall intensity estimation.
3) Over both land and ocean, large snowfall intensity underestimation exists for all 11 sensors, regardless of using either KuPR or CPR as the reference. This underestimation has strong effects for the broader end-user community due to its propagation to level3 merged precipitation products (e.g., IMERG; Wen et al. 2016; Behrangi et al. 2018; Sadeghi et al. 2019). The underestimation from the GMI retrieval over CONUS has also been reported by Mroz et al. (2021).

Note that the conclusions drawn from the comparison in this study are relevant to the version of the GPROF algorithm we examined (version 5) and are not indicative of the potential power of each of these sensors if different retrieval algorithms (potentially including future GPROF versions) were applied to them. In fact, other retrieval algorithms (e.g., Meng et al. 2017) showed that the low-frequency channels from ATMS (23, 31, and ~50 GHz) and AMSU-A also contain valuable snowfall

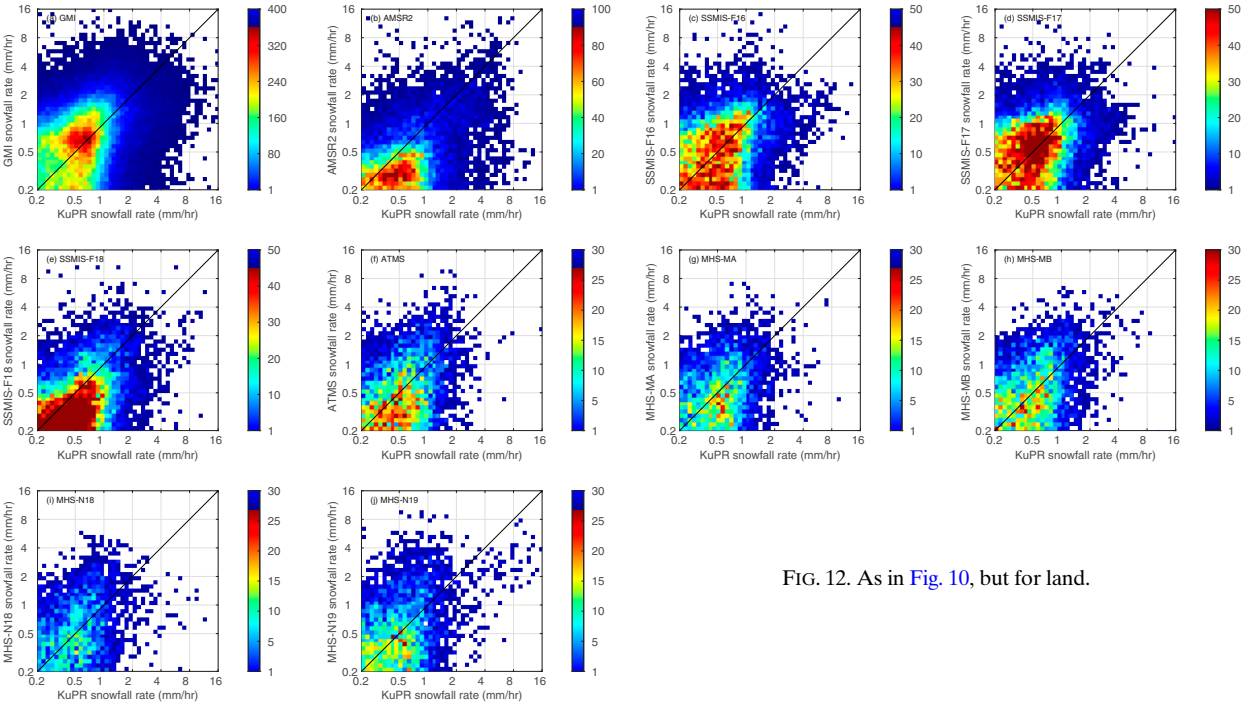

FIG. 12. As in Fig. 10, but for land.

retrieval information, which has not been exploited by the current version of GPROF algorithm for cross-track scanning radiometers. In addition, comparing the snowfall retrieval results from GPROF in this study and other previously published snowfall retrieval studies, it is possible that assigning higher weights for channels above 89 GHz (e.g., 150, 166, 183.3) may achieve better estimates (You et al. 2015, 2016; Meng et al. 2017; Rysman et al. 2018; Adhikari et al. 2020; Vahedizade et al. 2021). Finally, GPROF uses snowfall estimates from the ground radar network over CONUS to build the a priori database over the snow covered surface, which contributes to the large detection and intensity estimation uncertainties in the GPROF algorithm. It is shown that using CPR snowfall estimation can significantly improve the snowfall detection and intensity estimation performance (Mroz et al. 2021).

Acknowledgments. All passive microwave data and GPM KuPR data are downloaded from NASA Precipitation Processing System (PPS) website (https://storm.pps.eosdis.nasa.gov/storm/). The *CloudSat* snowfall product is downloaded from the CloudSat Data Processing Center at https://www.cloudsat.cira.colostate.edu/. This work is supported by the NASA Grant 80NSSC20K0903 from the Weather and Atmospheric Dynamics program and NASA's Precipitation Measurement Missions Program science team via the Internal Scientist Funding Model awarded to Dr. George Huffman. Y.Y. also would like to acknowledge the financial support from NOAA Grant NA19NES4320002 (Cooperative Institute for Satellite Earth System Studies-CICESS) at the University of Maryland/ESSIC.

Data availability statement. Data analyzed in this study are publicly available at PPS (https://storm.pps.eosdis.nasa.gov/storm/) and *CloudSat* (https://www.cloudsat.cira.colostate.edu/) website. The satellite matchups are available upon request by contacting Yalei You at youy@uncw.edu.

REFERENCES

Adhikari, A., M. R. Ehsani, Y. Song, and A. Behrangi, 2020: Comparative assessment of snowfall retrieval from microwave humidity sounders using machine learning methods. *Earth Space Sci.*, **7**, e2020EA001357, https://doi.org/10.1029/2020EA001357.

Behrangi, A., Y. Tian, B. H. Lambrigtsen, and G. L. Stephens, 2014: What does CloudSat reveal about global land precipitation detection by other spaceborne sensors? *Water Resour. Res.*, **50**, 4893–4905, https://doi.org/10.1002/2013WR014566.

——, K. J. Bormann, and T. H. Painter, 2018: Using the airborne snow observatory to assess remotely sensed snowfall products in the California Sierra Nevada. *Water Resour. Res.*, **54**, 7331–7346, https://doi.org/10.1029/2018WR023108.

Bennartz, R., and G. W. Petty, 2001: The sensitivity of microwave remote sensing observations of precipitation to ice particle size distributions. *J. Appl. Meteor. Climatol.*, **40**, 345–364, https://doi.org/10.1175/1520-0450(2001)040<0345:TSOMRS>2.0.CO;2.

Casella, D., G. Panegrossi, P. Sanò, A. C. Marra, S. Dietrich, B. T. Johnson, and M. S. Kulie, 2017: Evaluation of the GPM-DPR snowfall detection capability: Comparison with CloudSat-CPR. *Atmos. Res.*, **197**, 64–75, https://doi.org/10.1016/j.atmosres.2017.06.018.

Chen, F. W., and D. H. Staelin, 2003: AIRS/AMSU/HSB precipitation estimates. *IEEE Trans. Geosci. Remote Sens.*, **41**, 410–417, https://doi.org/10.1109/TGRS.2002.808322.

Chen, S., and Coauthors, 2016: Comparison of snowfall estimates from the NASA CloudSat cloud profiling radar and NOAA/

NSSL multi-radar multi-sensor system. *J. Hydrol.*, **541**, 862–872, https://doi.org/10.1016/j.jhydrol.2016.07.047.

Conner, M. D., and G. W. Petty, 1998: Validation and intercomparison of SSM/I rain-rate retrieval methods over the continental United States. *J. Appl. Meteor. Climatol.*, **37**, 679–700, https://doi.org/10.1175/1520-0450(1998)037<0679:VAIOSI>2.0.CO;2.

Eriksson, P., R. Ekelund, J. Mendrok, M. Brath, O. Lemke, and S. A. Buehler, 2018: A general database of hydrometeor single scattering properties at microwave and sub-millimetre wavelengths. *Earth Syst. Sci. Data*, **10**, 1301–1326, https://doi.org/10.5194/essd-10-1301-2018.

Foster, J. L., and Coauthors, 2012: Passive microwave remote sensing of the historic February 2010 snowstorms in the middle Atlantic region of the USA. *Hydrol. Processes*, **26**, 3459–3471, https://doi.org/10.1002/hyp.8418.

Gelaro, R., and Coauthors, 2017: The Modern-Era Retrospective Analysis for Research and Applications, version 2 (MERRA-2). *J. Climate*, **30**, 5419–5454, https://doi.org/10.1175/JCLI-D-16-0758.1.

Grody, N. C., 1991: Classification of snow cover and precipitation using the special sensor microwave imager. *J. Geophys. Res.*, **96**, 7423–7435, https://doi.org/10.1029/91JD00045.

Huffman, G. J., D. T. Bolvin, D. Braithwaite, K. Hsu, R. Joyce, P. Xie, and S.-H. Yoo, 2015: NASA Global Precipitation Measurement (GPM) Integrated Multi-satellite retrievals for GPM (IMERG). Algorithm Theoretical Basis Doc., version 4.5, 30 pp., http://pmm.nasa.gov/sites/default/files/document_files/IMERG_ATBD_V4.5.pdf.

Kongoli, C., P. Pellegrino, R. R. Ferraro, N. C. Grody, and H. Meng, 2003: A new snowfall detection algorithm over land using measurements from the Advanced Microwave Sounding Unit (AMSU). *Geophys. Res. Lett.*, **30**, 1756, https://doi.org/10.1029/2003GL017177.

——, H. Meng, J. Dong, and R. Ferraro, 2015: A snowfall detection algorithm over land utilizing high-frequency passive microwave measurements—Application to ATMS. *J. Geophys. Res. Atmos.*, **120**, 1918–1932, https://doi.org/10.1002/2014JD022427.

——, ——, ——, and ——, 2018: A hybrid snowfall detection method from satellite passive microwave measurements and global forecast weather models. *Quart. J. Roy. Meteor. Soc.*, **144**, 120–132, https://doi.org/10.1002/qj.3270.

Kubota, T., and Coauthors, 2007: Global precipitation map using satellite-borne microwave radiometers by the GSMaP project: Production and validation. *IEEE Trans. Geosci. Remote Sens.*, **45**, 2259–2275, https://doi.org/10.1109/TGRS.2007.895337.

Kulie, M. S., and R. Bennartz, 2009: Utilizing spaceborne radars to retrieve dry snowfall. *J. Appl. Meteor. Climatol.*, **48**, 2564–2580, https://doi.org/10.1175/2009JAMC2193.1.

——, ——, T. J. Greenwald, Y. Chen, and F. Weng, 2010: Uncertainties in microwave properties of frozen precipitation: Implications for remote sensing and data assimilation. *J. Atmos. Sci.*, **67**, 3471–3487, https://doi.org/10.1175/2010JAS3520.1.

——, L. Milani, N. B. Wood, S. A. Tushaus, R. Bennartz, and T. S. L'Ecuyer, 2016: A shallow cumuliform snowfall census using spaceborne radar. *J. Hydrometeor.*, **17**, 1261–1279, https://doi.org/10.1175/JHM-D-15-0123.1.

——, and Coauthors, 2021: Snowfall in the northern Great Lakes: Lessons learned from a multi-sensor observatory. *Bull. Amer. Meteor. Soc.*, **102**, E1317–E1339, https://doi.org/10.1175/BAMS-D-19-0128.1.

Kummerow, C. D., D. L. Randel, M. Kulie, N.-Y. Wang, R. Ferraro, S. J. Munchak, and V. Petkovic, 2015: The evolution of the Goddard profiling algorithm to a fully parametric scheme. *J. Atmos. Oceanic Technol.*, **32**, 2265–2280, https://doi.org/10.1175/JTECH-D-15-0039.1.

Kuo, K.-S., and Coauthors, 2016: The microwave radiative properties of falling snow derived from nonspherical ice particle models. Part I: An extensive database of simulated pristine crystals and aggregate particles, and their scattering properties. *J. Appl. Meteor. Climatol.*, **55**, 691–708, https://doi.org/10.1175/JAMC-D-15-0130.1.

Levizzani, V., S. Laviola, and E. Cattani, 2011: Detection and measurement of snowfall from space. *Remote Sens.*, **3**, 145–166, https://doi.org/10.3390/rs3010145.

Lin, X., and A. Y. Hou, 2008: Evaluation of coincident passive microwave rainfall estimates using TRMM PR and ground measurements as references. *J. Appl. Meteor. Climatol.*, **47**, 3170–3187, https://doi.org/10.1175/2008JAMC1893.1.

Liu, G., 2008a: A database of microwave single-scattering properties for nonspherical ice particles. *Bull. Amer. Meteor. Soc.*, **89**, 1563–1570, https://doi.org/10.1175/2008BAMS2486.1.

——, 2008b: Deriving snow cloud characteristics from CloudSat observations. *J. Geophys. Res.*, **113**, D00A09, https://doi.org/10.1029/2007JD009766.

——, and E.-K. Seo, 2013: Detecting snowfall over land by satellite high-frequency microwave observations: The lack of scattering signature and a statistical approach. *J. Geophys. Res. Atmos.*, **118**, 1376–1387, https://doi.org/10.1002/jgrd.50172.

Löhnert, U., S. Kneifel, A. Battaglia, M. Hagen, L. Hirsch, and S. Crewell, 2011: A multisensor approach toward a better understanding of snowfall microphysics: The TOSCA project. *Bull. Amer. Meteor. Soc.*, **92**, 613–628, https://doi.org/10.1175/2010BAMS2909.1.

Mätzler, C., 1994: Passive microwave signatures of landscapes in winter. *Meteor. Atmos. Phys.*, **54**, 241–260, https://doi.org/10.1007/BF01030063.

Meng, H., J. Dong, R. Ferraro, B. Yan, L. Zhao, C. Kongoli, N.-Y. Wang, and B. Zavodsky, 2017: A 1DVAR-based snowfall rate retrieval algorithm for passive microwave radiometers. *J. Geophys. Res. Atmos.*, **122**, 6520–6540, https://doi.org/10.1002/2016JD026325.

Michele, S. D., and P. Bauer, 2006: Passive microwave radiometer channel selection based on cloud and precipitation information content. *Quart. J. Roy. Meteor. Soc.*, **132**, 1299–1323, https://doi.org/10.1256/qj.05.164.

Milani, L., and N. B. Wood, 2021: Biases in CloudSat falling snow estimates resulting from daylight-only operations. *Remote Sens.*, **13**, 2041, https://doi.org/10.3390/rs13112041.

——, and Coauthors, 2021: Extreme lake-effect snow from a GPM microwave imager perspective: Observational analysis and precipitation retrieval evaluation. *J. Atmos. Oceanic Technol.*, **38**, 293–311, https://doi.org/10.1175/JTECH-D-20-0064.1.

Mroz, K., M. Montopoli, A. Battaglia, G. Panegrossi, P. Kirstetter, and L. Baldini, 2021: Cross validation of active and passive microwave snowfall products over the continental United States. *J. Hydrometeor.*, **22**, 1297–1315, https://doi.org/10.1175/JHM-D-20-0222.1.

Mugnai, A., and Coauthors, 2007: Snowfall measurements by proposed European GPM mission. *Measuring Precipitation from Space*, Springer, 655–674.

Munchak, S. J., and G. Skofronick-Jackson, 2013: Evaluation of precipitation detection over various surfaces from passive

microwave imagers and sounders. *Atmos. Res.*, **131**, 81–94, https://doi.org/10.1016/j.atmosres.2012.10.011.

Noh, Y.-J., G. Liu, E.-K. Seo, J. R. Wang, and K. Aonashi, 2006: Development of a snowfall retrieval algorithm at high microwave frequencies. *J. Geophys. Res.*, **111**, D22216, https://doi.org/10.1029/2005JD006826.

——, ——, A. S. Jones, and T. H. Vonder Haar, 2009: Toward snowfall retrieval over land by combining satellite and in situ measurements. *J. Geophys. Res.*, **114**, D24205, https://doi.org/10.1029/2009JD012307.

Norin, L., A. Devasthale, T. S. L'Ecuyer, N. B. Wood, and M. Smalley, 2015: Intercomparison of snowfall estimates derived from the CloudSat cloud profiling radar and the ground-based weather radar network over Sweden. *Atmos. Meas. Tech.*, **8**, 5009–5021, https://doi.org/10.5194/amt-8-5009-2015.

Panegrossi, G., J.-F. Rysman, D. Casella, A. C. Marra, P. Sanò, and M. S. Kulie, 2017: CloudSat-based assessment of GPM microwave imager snowfall observation capabilities. *Remote Sens.*, **9**, 1263, https://doi.org/10.3390/rs9121263.

Petty, G. W., and W. Huang, 2010: Microwave backscatter and extinction by soft ice spheres and complex snow aggregates. *J. Atmos. Sci.*, **67**, 769–787, https://doi.org/10.1175/2009JAS3146.1.

Prigent, C., F. Aires, and W. B. Rossow, 2006: Land surface microwave emissivities over the globe for a decade. *Bull. Amer. Meteor. Soc.*, **87**, 1573–1584, https://doi.org/10.1175/BAMS-87-11-1573.

Rysman, J.-F., G. Panegrossi, P. Sanò, A. C. Marra, S. Dietrich, L. Milani, and M. S. Kulie, 2018: SLALOM: An all-surface snow water path retrieval algorithm for the GPM microwave imager. *Remote Sens.*, **10**, 1278, https://doi.org/10.3390/rs10081278.

——, and Coauthors, 2019: Retrieving surface snowfall with the GPM microwave imager: A new module for the SLALOM algorithm. *Geophys. Res. Lett.*, **46**, 13 593–13 601, https://doi.org/10.1029/2019GL084576.

Sadeghi, L., B. Saghafian, and S. Moazami, 2019: Evaluation of IMERG and MRMS remotely sensed snowfall products. *Int. J. Remote Sens.*, **40**, 4175–4192, https://doi.org/10.1080/01431161.2018.1562259.

Sims, E. M., and G. Liu, 2015: A parameterization of the probability of snow–rain transition. *J. Hydrometeor.*, **16**, 1466–1477, https://doi.org/10.1175/JHM-D-14-0211.1.

Skofronick-Jackson, G. M., and B. T. Johnson, 2011: Surface and atmospheric contributions to passive microwave brightness temperatures for falling snow events. *J. Geophys. Res.*, **116**, D02213, https://doi.org/10.1029/2010JD014438.

——, M.-J. Kim, J. A. Weinman, and D.-E. Chang, 2004: A physical model to determine snowfall over land by microwave radiometry. *IEEE Trans. Geosci. Remote Sens.*, **42**, 1047–1058, https://doi.org/10.1109/TGRS.2004.825585.

——, B. T. Johnson, and S. J. Munchak, 2013: Detection thresholds of falling snow from satellite-borne active and passive sensors. *IEEE Trans. Geosci. Remote Sens.*, **51**, 4177–4189, https://doi.org/10.1109/TGRS.2012.2227763.

——, D. Kirschbaum, W. Petersen, G. Huffman, C. Kidd, E. Stocker, and R. Kakar, 2018: The Global Precipitation Measurement (GPM) mission's scientific achievements and societal contributions: Reviewing four years of advanced rain and snow observations. *Quart. J. Roy. Meteor. Soc.*, **144**, 27–48, https://doi.org/10.1002/qj.3313.

——, M. Kulie, L. Milani, S. J. Munchak, N. B. Wood, and V. Levizzani, 2019: Satellite estimation of falling snow: A Global Precipitation Measurement (GPM) *Core Observatory* perspective. *J. Appl. Meteor. Climatol.*, **58**, 1429–1448, https://doi.org/10.1175/JAMC-D-18-0124.1.

Song, Y., A. Behrangi, and E. Blanchard-Wrigglesworth, 2020: Assessment of satellite and reanalysis cold season snowfall estimates over Arctic sea ice. *Geophys. Res. Lett.*, **47**, e2020GL088970, https://doi.org/10.1029/2020GL088970.

Staelin, D. H., and F. W. Chen, 2000: Precipitation observations near 54 and 183 GHz using the NOAA-15 satellite. *IEEE Trans. Geosci. Remote Sens.*, **38**, 2322–2332, https://doi.org/10.1109/36.868889.

Stephens, G. L., and C. D. Kummerow, 2007: The remote sensing of clouds and precipitation from space: A review. *J. Atmos. Sci.*, **64**, 3742–3765, https://doi.org/10.1175/2006JAS2375.1.

Takbiri, Z., L. Milani, C. Guilloteau, and E. Foufoula-Georgiou, 2021: Quantitative investigation of radiometric interactions between snowfall, snow cover, and cloud liquid water over land. *Remote Sens.*, **13**, 2641, https://doi.org/10.3390/rs13132641.

Tang, G., D. Long, A. Behrangi, C. Wang, and Y. Hong, 2018: Exploring deep neural networks to retrieve rain and snow in high latitudes using multisensor and reanalysis data. *Water Resour. Res.*, **54**, 8253–8278, https://doi.org/10.1029/2018WR023830.

——, M. P. Clark, S. M. Papalexiou, Z. Ma, and Y. Hong, 2020: Have satellite precipitation products improved over last two decades? A comprehensive comparison of GPM IMERG with nine satellite and reanalysis datasets. *Remote Sens. Environ.*, **240**, 111697, https://doi.org/10.1016/j.rse.2020.111697.

Tang, L., Y. Tian, and X. Lin, 2014: Validation of precipitation retrievals over land from satellite-based passive microwave sensors. *J. Geophys. Res. Atmos.*, **119**, 4546–4567, https://doi.org/10.1002/2013JD020933.

Vahedizade, S., A. Ebtehaj, Y. You, S. E. Ringerud, and F. J. Turk, 2021: Passive microwave signatures and retrieval of high-latitude snowfall over open oceans and sea ice: Insights from coincidences of GPM and CloudSat satellites. *IEEE Trans. Geosci. Remote Sens.*, **60**, 1–13, https://doi.org/10.1109/TGRS.2021.3071709.

von Lerber, A., D. Moisseev, D. A. Marks, W. Petersen, A.-M. Harri, and V. Chandrasekar, 2018: Validation of GMI snowfall observations by using a combination of weather radar and surface measurements. *J. Appl. Meteor. Climatol.*, **57**, 797–820, https://doi.org/10.1175/JAMC-D-17-0176.1.

Wang, Y., G. Liu, E.-K. Seo, and Y. Fu, 2013: Liquid water in snowing clouds: Implications for satellite remote sensing of snowfall. *Atmos. Res.*, **131**, 60–72, https://doi.org/10.1016/j.atmosres.2012.06.008.

Wen, Y., A. Behrangi, B. Lambrigtsen, and P.-E. Kirstetter, 2016: Evaluation and uncertainty estimation of the latest radar and satellite snowfall products using SNOTEL measurements over mountainous regions in western United States. *Remote Sens.*, **8**, 904, https://doi.org/10.3390/rs8110904.

Wilks, D. S., 2011: *Statistical Methods in the Atmospheric Sciences*. 3rd ed. International Geophysics Series, Vol. 100, Academic Press, 704 pp.

Xie, P., R. Joyce, S. Wu, S.-H. Yoo, Y. Yarosh, F. Sun, and R. Lin, 2017: Reprocessed, bias-corrected CMORPH global high-resolution precipitation estimates from 1998. *J. Hydrometeor.*, **18**, 1617–1641, https://doi.org/10.1175/JHM-D-16-0168.1.

Xie, X., U. Löhnert, S. Kneifel, and S. Crewell, 2012: Snow particle orientation observed by ground-based microwave

radiometry. *J. Geophys. Res.*, **117**, D02206, https://doi.org/10.1029/2011JD016369.

Yang, J. X., D. S. McKague, and C. S. Ruf, 2016: Uncertainties in radiometer intercalibration associated with variability in geophysical parameters. *J. Geophys. Res. Atmos.*, **121**, 11 348–11 367, https://doi.org/10.1002/2016JD024937.

You, Y., and G. Liu, 2012: The relationship between surface rainrate and water paths and its implications to satellite rainrate retrieval. *J. Geophys. Res.*, **117**, D13207, https://doi.org/10.1029/2012JD017662.

——, N.-Y. Wang, and R. Ferraro, 2015: A prototype precipitation retrieval algorithm over land using passive microwave observations stratified by surface condition and precipitation vertical structure. *J. Geophys. Res. Atmos.*, **120**, 5295–5315, https://doi.org/10.1002/2014JD022534.

——, ——, ——, and P. Meyers, 2016: A prototype precipitation retrieval algorithm over land for ATMS. *J. Hydrometeor.*, **17**, 1601–1621, https://doi.org/10.1175/JHM-D-15-0163.1.

——, ——, ——, and S. Rudlosky, 2017: Quantifying the snowfall detection performance of the GPM Microwave Imager channels over land. *J. Hydrometeor.*, **18**, 729–751, https://doi.org/10.1175/JHM-D-16-0190.1.

——, V. Petkovic, J. Tan, R. Kroodsma, W. Berg, C. Kidd, and C. Peters-Lidard, 2020: Evaluation of V05 precipitation estimates from GPM constellation radiometers using KuPR as the reference. *J. Hydrometeor.*, **21**, 705–728, https://doi.org/10.1175/JHM-D-19-0144.1.

——, C. Peters-Lidard, S. Ringerud, and J. M. Haynes, 2021: Evaluation of rainfall-snowfall separation performance in remote sensing datasets. *Geophys. Res. Lett.*, **48**, e2021GL094180, https://doi.org/10.1029/2021GL094180.

——, H. Meng, J. Dong, Y. Fan, R. R. Ferraro, G. Gu, and L. Wang, 2022: A snowfall detection algorithm for ATMS over ocean, sea ice, and coast. *IEEE J. Sel. Top. Appl. Earth Obs. Remote Sens.*, **15**, 1411–1420, https://doi.org/10.1109/JSTARS.2022.3140768.